Molecular electronic spin qubit from a spin-frustrated trinuclear copper complex

Benjamin Kintzel, Michael Böhme, Junjie Liu, Anja Burkhardt, Jakub Mrozek, Axel Buchholz, Arzhang Ardavan, and Winfried Plass*

Electronic Supplementary Information (ESI)

Contents

List of Figures

List of Tables

S1   Materials and synthesis

All reagents were purchased from commercial sources at reagent grade and used without further purification. Solvents were distilled once from CaH_2 prior to use except for dmf which was only distilled. H_5saltag $\cdot$ HCl was prepared as reported in literature.[1]

Caution! *Perchlorate derivatives may detonate upon scraping or heating.*

Synthesis of [Cu$_3$(saltag)(py)$_6$]ClO$_4$ (Cu$_3$saltag)

$Cu(ClO_4)_2 \cdot 6 H_2O$ (619 mg, 1.67 mmol) and H_5saltag $\cdot$ HCl (252 mg, 0.56 mmol) were dissolved in dmf (50 mL) under mild heating. A solution of triethylamine (340 mg, 3.36 mmol) in dmf (5 mL) was added and the whole mixture transferred dropwise over 30 min into refluxing MeOH (30 mL) followed by the subsequent addition of dmf (5 mL) and MeOH (20 mL) to the still boiling reaction mixture. After further refluxing for 5 min the suspension was slowly cooled down to 3 °C and maintained at this temperature for several hours. The precipitated green solid was filtered off, washed with MeOH and dried at air overnight to give an amorphous precursor material for the subsequent crystallization of the title compound. This precursor material was suspended in EtOH (20 mL) and under reflux conditions the same volume of pyridine (20 mL) was added stepwise over a period of 5 min followed by further 30 min of heating. The hot suspension was filtered and the filtrate subsequently cooled to −25 °C (with intermediate steps at 3 °C and −10 °C each maintained for about 24 h) to give a first crop of very small dark green crystals (yield ≈ 50 mg). Heating the solid remaining in the filter in pyridine gave a saturated solution of the complex, which was subsequently filtered at room-temperature and layered with an EtOH solution of $NaClO_4$. Slow diffusion of the layers at room temperature afforded additional crystalline product. For analytical characterization solely crystalline product was used.

ESI-MS (pos., MeOH): m/z = 634 (40%, [Cu$_3$(saltag) $\cdot$ MeOH]$^+$), 666 (100%, [Cu$_3$(saltag) $\cdot$ 2 MeOH]$^+$), 698 (25%, [Cu$_3$(saltag) $\cdot$ 3 MeOH]$^+$).

Elemental Analysis: Calcd for **Cu$_3$saltag**$\cdot$1/2([Hpy]ClO$_4$) $C_{54.5}H_{48}N_{12.5}Cu_3Cl_{1.5}O_9$ (1265.86 g cm^{-3}): C 51.71; H 3.82; N 13.83%. Found: C 52.03; H 3.82; N 14.03%.

IR (ATR, selected bands, cm^{-1}): 3058 (w, ν(C–H)), 3017 (w, ν(C–H)), 1596 (s), 1478/1463/1443 (vs), 1361 (s), 1198 (s), 1095/1065 (vs), 751 (s), 697 (vs).

S2 Crystal structure details

Single crystals were selected under a stereo microscope, mounted on cryogenic loops and were flash-frozen in liquid N_2. Diffraction data were collected at DESY beamline P11 at PETRA III, Hamburg, Germany[2] using a Pilatus 6M detector (Dectris AG, Switzerland). An X-ray beam with a photon flux of 5×10^9 photons s^{-1} at an X-ray energy of 20.00 keV ($\lambda = 0.6199$Å) was used for the experiment. Full rotation series of 720 images per crystal were collected at a sample-to-detector distance of 156 mm, a rotation range of 0.5° and an exposure time of 250 ms per frame. During data collection the temperature was adjusted to 80 K via an open-flow nitrogen cryostat (Oxford Cryosystems Ltd, United Kingdom) in order to minimize X-ray induced radiation damage. Indexing and integration was carried out using the XDS program package.[3] The structure was solved by direct methods (SHELXS) and refined by full-matrix least-squares techniques against F^2 (SHELXL).[4] CIF is deposited as CCDC 1862694.

X-ray powder diffraction (XRPD):   X-ray diffraction measurements on powdered samples were performed on a Stoe Powder Diffractometer with a Mythen 1K detector at room temperature. Measurements were done using capillary tubes while the Debye Scherrer Scan Mode was applied with a 2θ scan type. The X-ray tube was a Cu-long fine focus tube. The measurement was carried out between 2 and 50° with steps of 2.1° per 20 seconds.

Table S1: Crystallographic data and structure refinement parameters.

formula	$C_{54.5}H_{50}Cl_{1.5}Cu_3N_{12.5}O_{10}$
formula weight ($g\,mol^{-1}$)	1283.86
crystal system	trigonal
space group	$P31c$
a (pm)	1506.4(2)
b (pm)	1506.4(2)
c (pm)	2904.2(6)
α (°)	90
β (°)	90
γ (°)	120
V ($10^6\,pm^3$)	5707(2)
T (K)	80(2)
δ_{calc} ($g\,cm^{-3}$)	1.494
Z	4
μ (mm^{-1})	0.862
Flack parameter	0.056(3)
wavelength (pm)	61.99
radiation type	synchrotron
Θ range of data collection (°)	$1.492 \leq \Theta \leq 27.112$
measured reflections	113617
independent reflections	12610
reflections used	12271
R_{int}	0.0380
no. of parameters	527
no. of restraints	7
goodness-of-fit	1.070
R_1 (all data)	0.0392
R_1	0.0383
wR_2 (all data)	0.1152
wR_2	0.1141
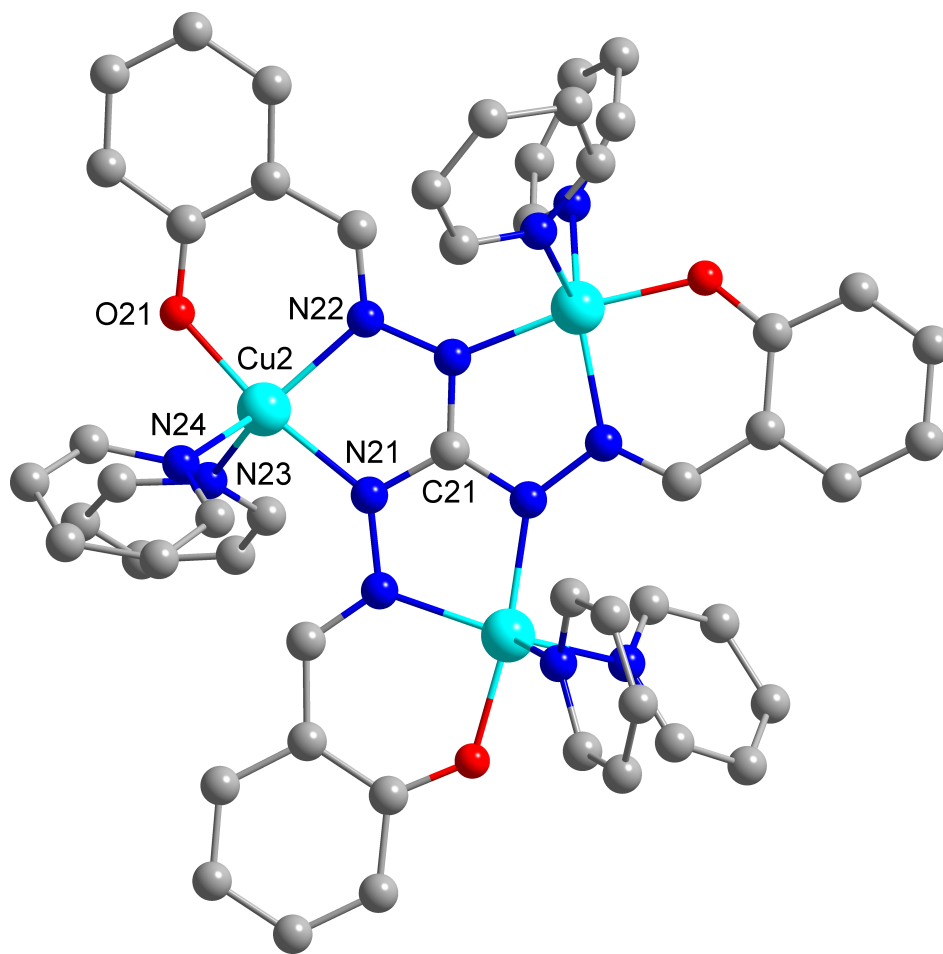
Fig. S1: Molecular structure of the second crystallographically independent cationic complex [Cu$_3$(saltag)(py)$_6$]$^+$ in the crystal structure of **Cu$_3$saltag**. Hydrogen atoms are omitted for clarity.
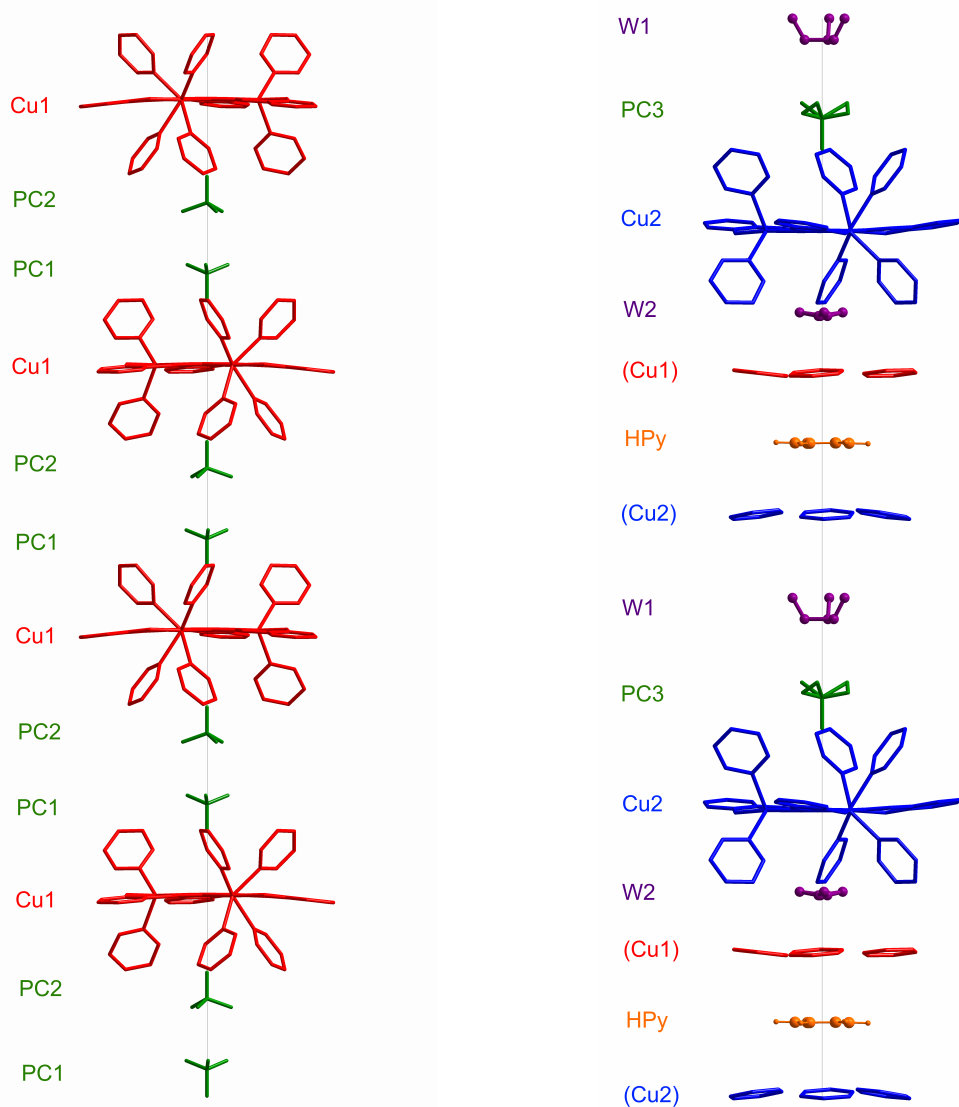
Fig. S2: The unit cell contains two distinct crystallographic 3-fold axes, along which the molecules of Cu1 (left, red – 3-fold axis at the intersection of the axial glide planes) and Cu2 (right, blue) are aligned. Depicted is the side view on both axes along the crystallographic *b* axis. In case of Cu1 (left, red – 3-fold axis at the intersection of the axial glide planes) two perchlorate anions (PC1 and PC2, green) are alternating with the complex cation along the axis. For Cu2 (right, blue) an alternating stacked arrangement is observed with the remaining perchlorate anion (PC3, green), a water molecule (W1, violet, disordered), symmetrically shifted Cu2 complex cations (blue), the pyridinium cation (Hpy, orange), symmetrically shifted Cu1 complex cations (red), and a second water molecule (W2, violet, disordered). Hydrogen atoms are omitted for clarity.
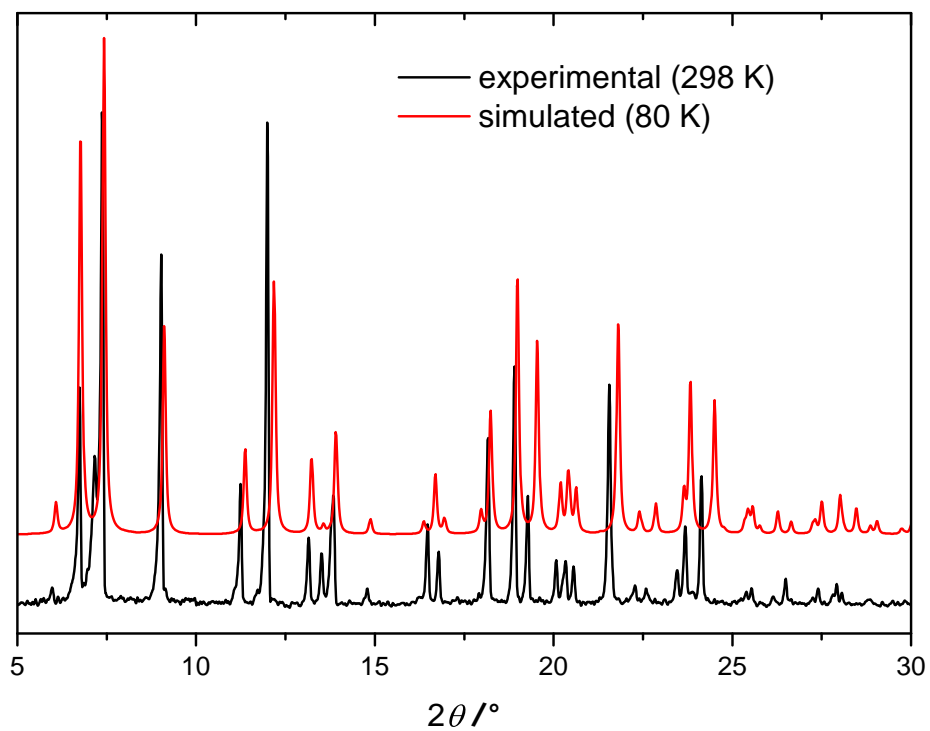
Fig. S3: X-ray diffraction powder pattern for **Cu₃saltag** (black) and the powder pattern simulated from the single crystal data (red). Slight shifts of reflections are due to the difference in temperature.
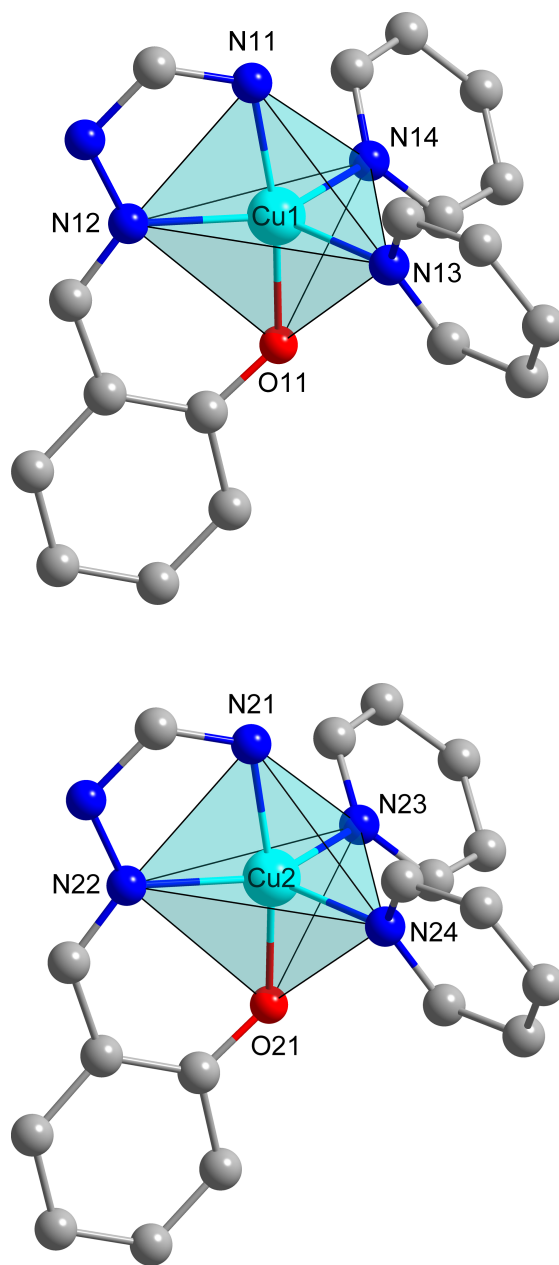
Fig. S4: Representation of the tigonal bipyramidal coordination polyhedra for the copper(II) centers Cu1 (top) and Cu2 (bottom) of **Cu₃saltag**. Hydrogen atoms are omitted for clarity.

Table S2: Selected bond lengths (in pm) and angles (in °) for both complex cations $[Cu_3(saltag)(py)_6]^+$.

	$n = 1$	$n = 2$
Cun–On1	190.7(3)	190.0(2)
Cun–Nn1[a]	197.4(3)	197.9(3)
Cun–Nn2	198.6(3)	198.8(3)
Cun–Nn3	218.5(3)	211.9(3)
Cun–Nn4	212.9(3)	217.4(3)
On1–Cun–Nn1[a]	171.39(11)	170.77(11)
On1–Cun–Nn2	92.51(11)	92.02(10)
On1–Cun–Nn3	91.21(11)	87.96(11)
On1–Cun–Nn4	88.13(12)	92.15(11)
Nn1[a]–Cun–Nn2	79.38(11)	79.78(11)
Nn1[a]–Cun–Nn3	95.67(11)	95.07(11)
Nn1[a]–Cun–Nn4	95.55(12)	95.71(11)
Nn2–Cun–Nn3	123.39(12)	136.53(11)
Nn2–Cun–Nn4	135.11(12)	121.20(11)
Nn4–Cun–Nn3	101.46(11)	102.22(11)

[a] Atom generated by symmetry operation:

$n = 1$: $-1 - y, 1 + x - y, +z$;

$n = 2$: $-1 + y - x, -x, +z$
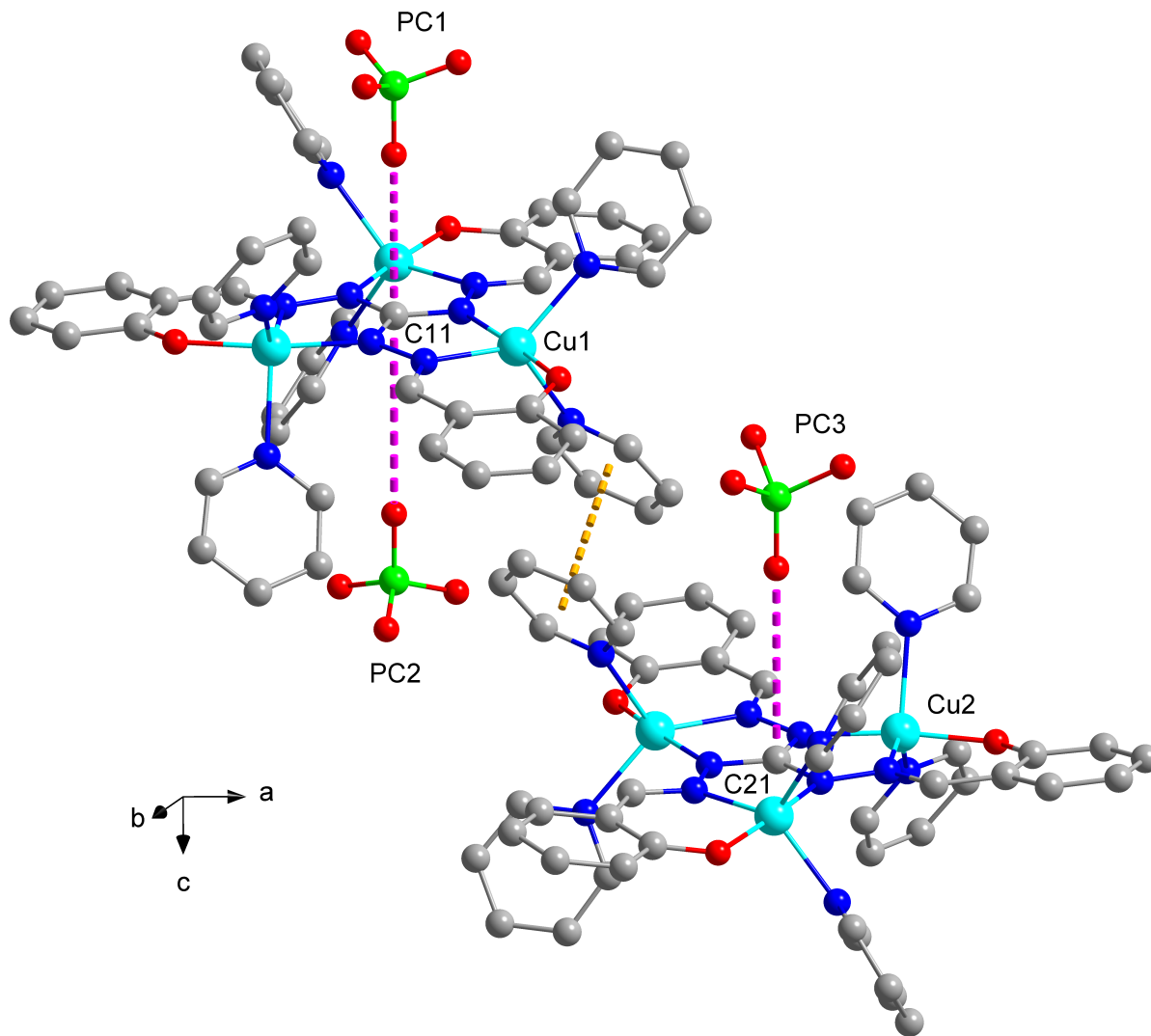
Fig. S5: Representation of intermolecular interactions for the two cationic complex molecules $[Cu_3(saltag)(py)_6]^+$ in the crystal structure of **Cu$_3$saltag**. The π-π interaction is shown as yellow dashed line (distances: inter-plane 346 pm; centroid···centroid 365 pm). Ionic interactions of the cationic complexes with the perchlorate counterions are depicted as pink dashed lines (perchlorate···Cn1).

Table S3: Selected distances (in pm) for the interactions of the three perchlorate counterions PC1–PC3 with the cationic complex molecules of **Cu$_3$saltag** (see also Fig. S5).

	PC1 $(i = 1, n = 1)$	PC2 $(i = 2, n = 1)$	PC3 $(i = 3, n = 2)$
Cli–OPi1	147.5(17)	143.3(9)	153.4(12)
Cli–OPi2	136.4(12)	141.7(12)	152.5(11)
OPi1···Cn1	346.8(16)	426.3(11)	412.1(13)

S12
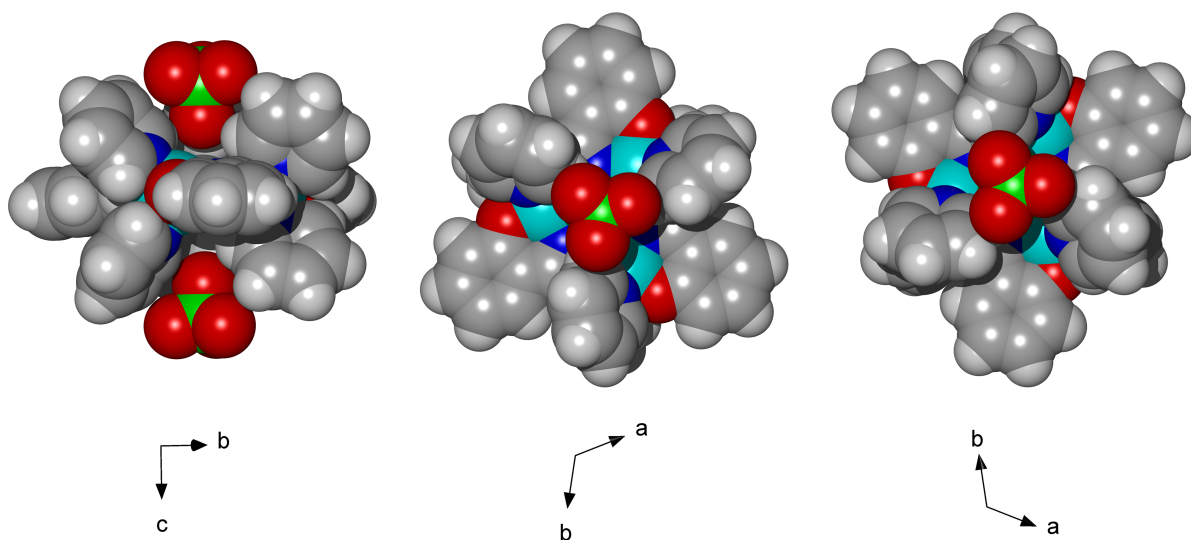
Fig. S6: Space-filling model for the complex molecule of Cu1 together with the two encapsulated perchlorate anions from different orientations (left: side view; center: top view; right: bottom view).
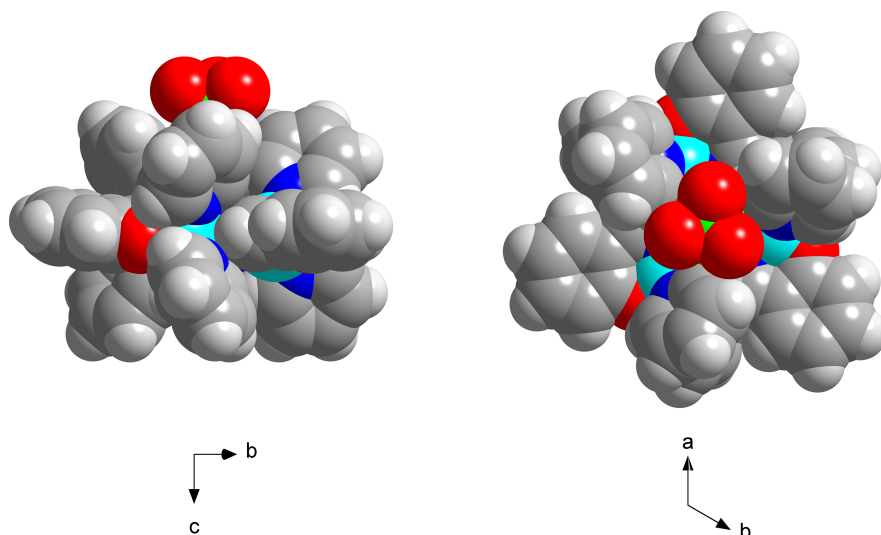
Fig. S7: Space-filling model for the complex molecule of Cu2 together with the encapsulated perchlorate anion from different directions (left: side view; right: top view).

S3 Theoretical studies on intermolecular interactions

Computational details for interaction studies: The atomic positions for the structures used in the DFT-D3 studies were taken from the single-crystal structure data. The positions of all hydrogen atoms were optimized with the Turbomole[5] package of programs at RI-DFT[6]/BP86[7,8]/def2-SVP[9] level of theory. Within these geometry optimizations a C_3 symmetry was used together with a replacement of all copper(II) ions by diamagnetic zinc(II) ions to achieve a faster convergence in the self-consistent field steps. The single-point energies for the geometry optimized structures have been obtained at the DFT/B3-LYP[7,10]/def2-TZVPP[9] level of theory utilizing the molecular C_3 symmetry and employing Grimme's dispersion correction D3.[11] Moreover, a counterpoise correction as suggested by Boys[12] was employed to minimize the so-called basis set superposition error. The final energies are listed in Table S4, where the necessary calculations for the counterpoise correction are marked with an asterisk. The structures of the computational models to calculate the $ClO_4 \cdots py$ interaction energies are depicted in Fig. S8.

Computational details for geometry optimization studies: The atomic coordinates for the starting structures used in the DFT-D3 geometry optimization studies were taken from the crystal structure data of the trinuclear complex based on Cu1. Full geometry optimizations including the position of all atoms were performed for the high-spin state ($S = 3/2$) of the trinuclear complexes at the RI-DFT-D3[6,11]/BP86[7,8]/def2-TZVPP[9] level of theory employing a C_3 molecular symmetry. The obtained final structures for the trinuclear complexes with and without perchlorate interactions are depicted in Fig. S9. The presence of at least one perchlorate anion seems to stabilize the trigonal bipyramidal geometry at the copper(II) centers.

Table S4: DFT-D3/B3LYP/def2-TZVPP results for the calculation of the $ClO_4 \cdots Cn1$ interaction energies (for notation see Fig. S5). Asterisks indicate the inclusion of a counterpoise correction (see text).

computational model	basis functions	atoms	$2S+1$	$E_{\text{DFT-D3}}$ (a.u.)
Cu1	2899	115	4	-7812.18721
PC1	166	5	1	-760.84530
Cu1$\cdots$PC1	3065	120	4	-8573.14578
Cu1$\cdots$(PC1)*	3065	115	4	-7812.18737
(Cu1)$^* \cdots$PC1	3065	5	1	-760.84838
PC2	166	5	1	-760.86958
Cu1$\cdots$PC2	3065	120	4	-8573.16024
Cu1$\cdots$(PC2)*	3065	115	4	-7812.18734
(Cu1)$^* \cdots$PC2	3065	5	1	-760.87244
Cu2	2899	115	4	-7812.18941
PC3	166	5	1	-760.81922
Cu2$\cdots$PC3	3065	120	4	-8573.10883
Cu2$\cdots$(PC3)*	3065	115	4	-7812.18953
(Cu2)$^* \cdots$PC3	3065	5	1	-760.82293

Table S5: DFT-D3/B3LYP/def2-TZVPP results for the calculation of the $ClO_4 \cdots py$ interaction energies utilizing the model structures depicted in Fig. S8 (for notation see Fig. S5). Asterisks indicate the inclusion of a counterpoise correction (see text).

computational model	basis functions	atoms	$2S+1$	$E_{\text{DFT-D3}}$ (a.u.)
PC1	166	5	1	-760.84530
$(py)_3$	768	33	1	-744.68343
PC1$\cdots(py)_3$	934	38	1	-1505.55909
PC1$\cdots((py)_3)^*$	934	5	1	-760.84822
$(PC1)^*\cdots(py)_3$	934	33	1	-744.68354
PC2	166	5	1	-760.86958
$(py)_3$	768	33	1	-744.68695
PC2$\cdots(py)_3$	934	38	1	-1505.58207
PC2$\cdots((py)_3)^*$	934	5	1	-760.87232
$(PC2)^*\cdots(py)_3$	934	33	1	-744.68707
PC3	166	5	1	-760.81922
$(py)_3$	768	33	1	-744.68549
PC3$\cdots(py)_3$	934	38	1	-1505.52976
PC3$\cdots((py)_3)^*$	934	5	1	-760.82277
$(PC3)^*\cdots(py)_3$	934	33	1	-744.68560

PC1$\cdots(py)_3$ PC2$\cdots(py)_3$ PC3$\cdots(py)_3$
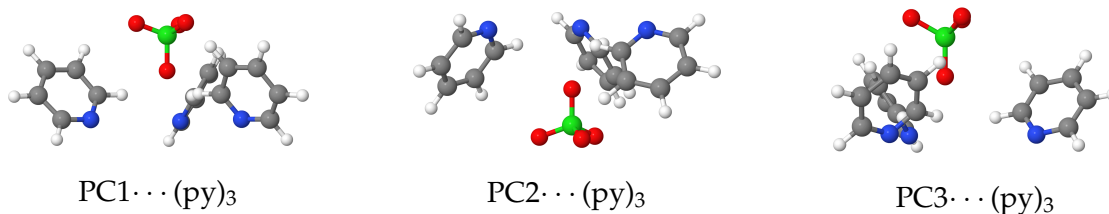
Fig. S8: Computational models for the calculations of the $ClO_4 \cdots py$ interaction energies.
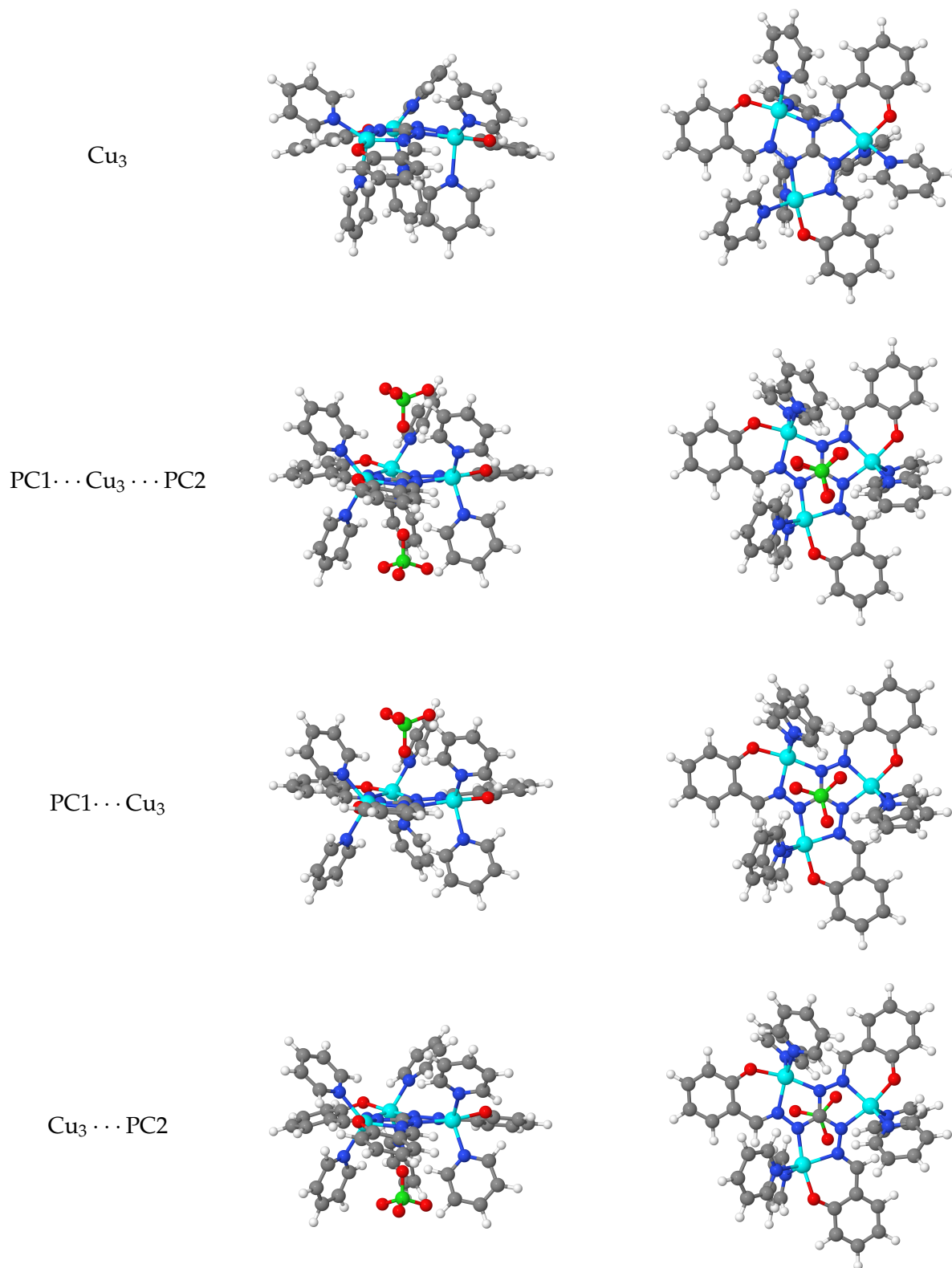
Fig. S9: DFT-optimized structures of the trinuclear copper(II) complex for models with (PC1···Cu$_3$···PC2, PC1···Cu$_3$, Cu$_3$···PC2) and without (Cu$_3$) interacting perchlorate anions (PC1 and PC2) with side (left column) and top view (right column) for each structure.

S4   Packing diagrams and π-π interactions
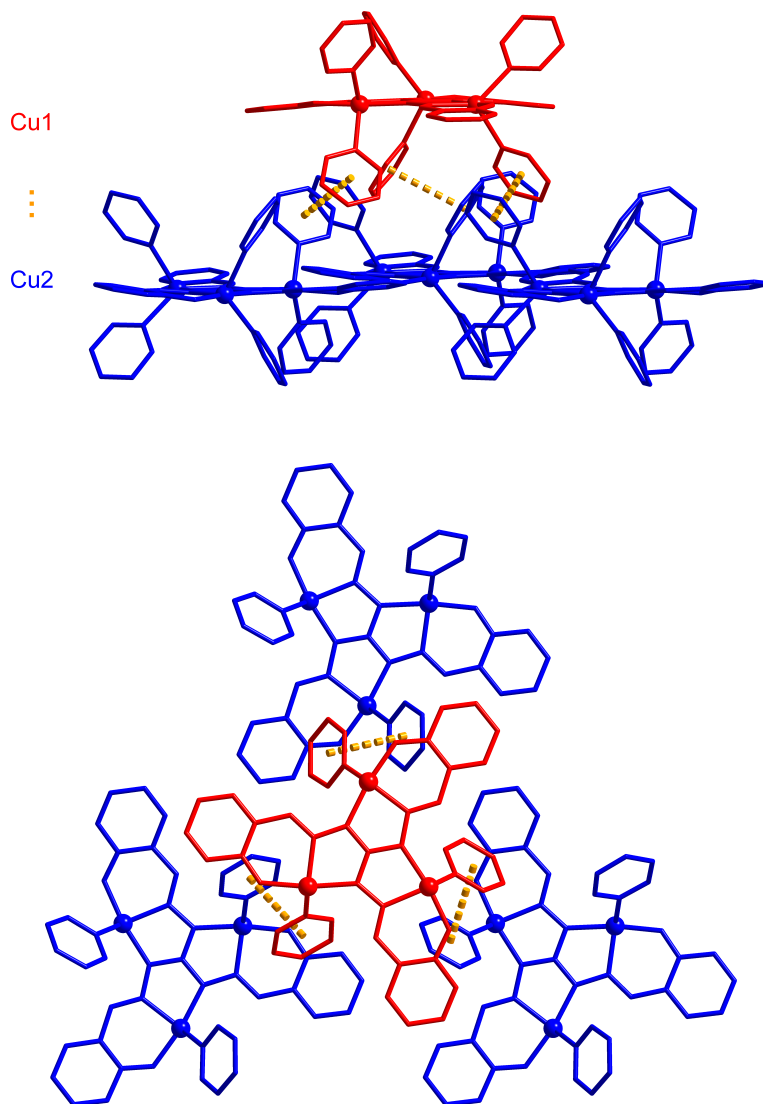
Fig. S10: Representation of π-π interactions (dashed orange lines) between the trinuclear cationic complex Cu1 (red) and its three adjacent cationic complex Cu2 (blue) as view along the 3-fold axis (bottom) and side view (top). Hydrogen atoms and pyridine co-ligands not involved in π-π interactions are omitted for clarity.
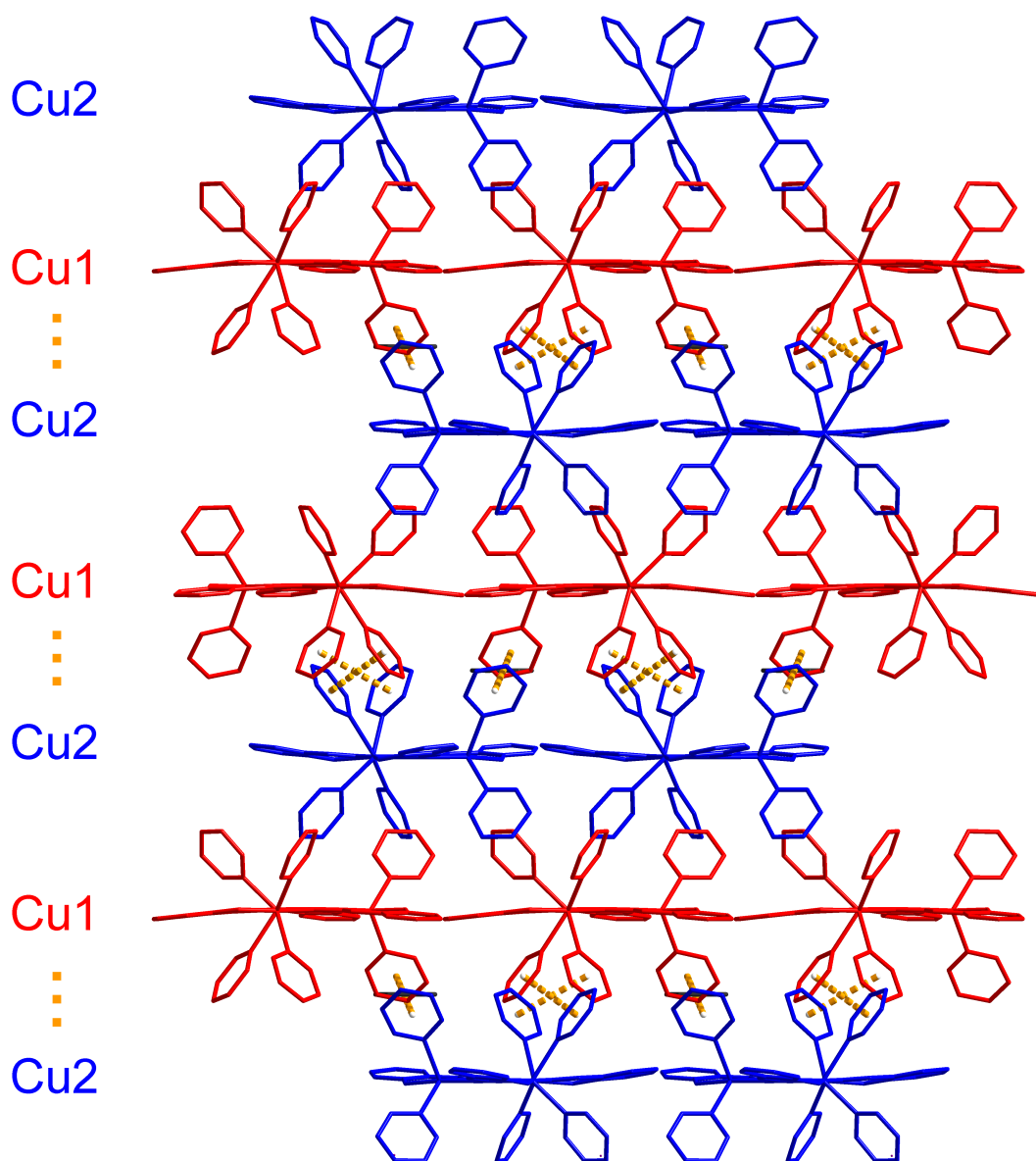
Fig. S11: Packing diagram of **Cu₃saltag** with a view along the crystallographic b axis. The color code represents the two different cationic trinuclear copper(II) complexes based on Cu1 (red) and Cu2 (blue). The intermolecular π-π interactions are shown as orange dashed lines. Hydrogen atoms as well as additional water, pyridinium, and perchlorate molecules are omitted for clarity.

S5 Magnetic susceptibility data

Instrumentation: Magnetic measurements were performed on a Quantum Design MPMS-5 SQUID magnetometer. Susceptibility data were obtained in the temperature range from 2 to 300 K for a polycrystalline sample, which was placed in a gelatine capsule. The collected data were corrected for the diamagnetism of the sample holder, the capsule, and the diamagnetic contribution of the ligand.

Fit details: Fitting of the magnetic susceptibility data was performed using PHI program package.[13] During the fit correction terms for temperature independent contributions (χ_{tic}) and intermolecular exchange interactions (zJ) were included. An equilateral triangle was applied as spin topology (see Fig. S12), resulting in the parameters given in Table S6.
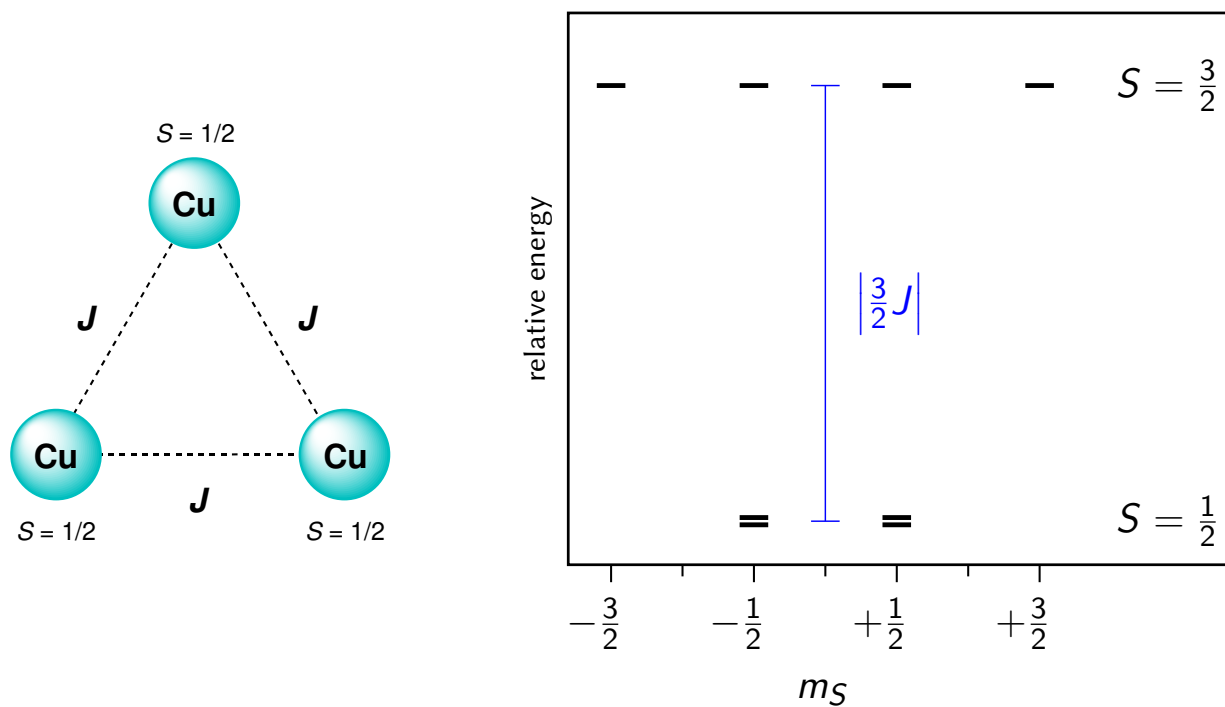
Fig. S12: Coupling scheme (left) used for the fit of the magnetic susceptibility data of **Cu₃saltag** and the resulting spin states (right) assuming an antiferromagnetic coupling ($J < 0$).

Table S6: Magnetic parameters for **Cu₃saltag** obtained by the fit of the susceptibility data to eqn (1) from the main manuscript.

g	J (cm^{-1})	zJ (cm^{-1})	χ_{tic} (cm^3 mol^{-1})
2.155(1)	−297.8(5)	−0.048(3)	0.143(2) $\cdot$ 10^{-3}

Low temperature behavior and antisymmetric exchange (ASE): To probe the origin of the low temperature behavior of the system additional fitting attempts including effects from antisymmetric exchange interactions (ASE) as well as intermolecular exchange interactions (zJ). For this purpose the Hamiltonian given in eqn (1) of the main manuscript was extended by the term given in eqn (S1), which exclusively considers the z-component due to the strict trigonal symmetry ($G_z \gg G_x, G_y \approx 0$).

$$\hat{H} = G_z \left[(\hat{S}_{1,x}\hat{S}_{2,y} - \hat{S}_{1,y}\hat{S}_{2,x}) + (\hat{S}_{2,x}\hat{S}_{3,y} - \hat{S}_{2,y}\hat{S}_{3,x}) + (\hat{S}_{3,x}\hat{S}_{1,y} - \hat{S}_{3,y}\hat{S}_{1,x}) \right] \tag{S1}$$

Three different fitting attempts have been performed including either the antisymmetric exchange (ASE), the intermolecular interaction term (zJ) or both interactions simultaneously (zJ and ASE). The corresponding data summarized in S7 clearly indicates that the intermolecular interaction term best describes the low temperature behavior. In fact, for the simultaneous fit the contribution of the antisymmetric exchange is virtually undefined as indicated by the extremely large error margin. Therefore, it can be concluded that the antisymmetric exchange only gives rise to a very minor contribution in the case of **Cu₃saltag**, assumed to be well below the upper limit given by the fit only considering antisymmetric exchange (ASE).

Table S7: Comparison of magnetic parameters for **Cu₃saltag** obtained by the fit of the susceptibility data with respect to a possible antisymmetric exchange (ASE) and mean-field intermolecular exchange interaction (MF).

	MF	MF and ASE	ASE
g	2.1557(6)	2.1557(6)	2.1470(8)
$J/$ cm^{-1}	$-297.8(3)$	$-297.8(3)$	$-304.0(4)$
$G_z/$ cm^{-1}	-	$4(20000) \cdot 10^{-5}$	$-0.97(7)$
$\chi_{tic}/$ cm^{3}mol^{-1}	$1.43(2) \cdot 10^{-4}$	$1.43(2) \cdot 10^{-4}$	$1.82(3) \cdot 10^{-2}$
$zJ/$ cm^{-1}	$-0.048(3)$	$-0.048(3)$	-
Residual	$6.67 \cdot 10^{-5}$	$6.67 \cdot 10^{-5}$	$1.47 \cdot 10^{-3}$
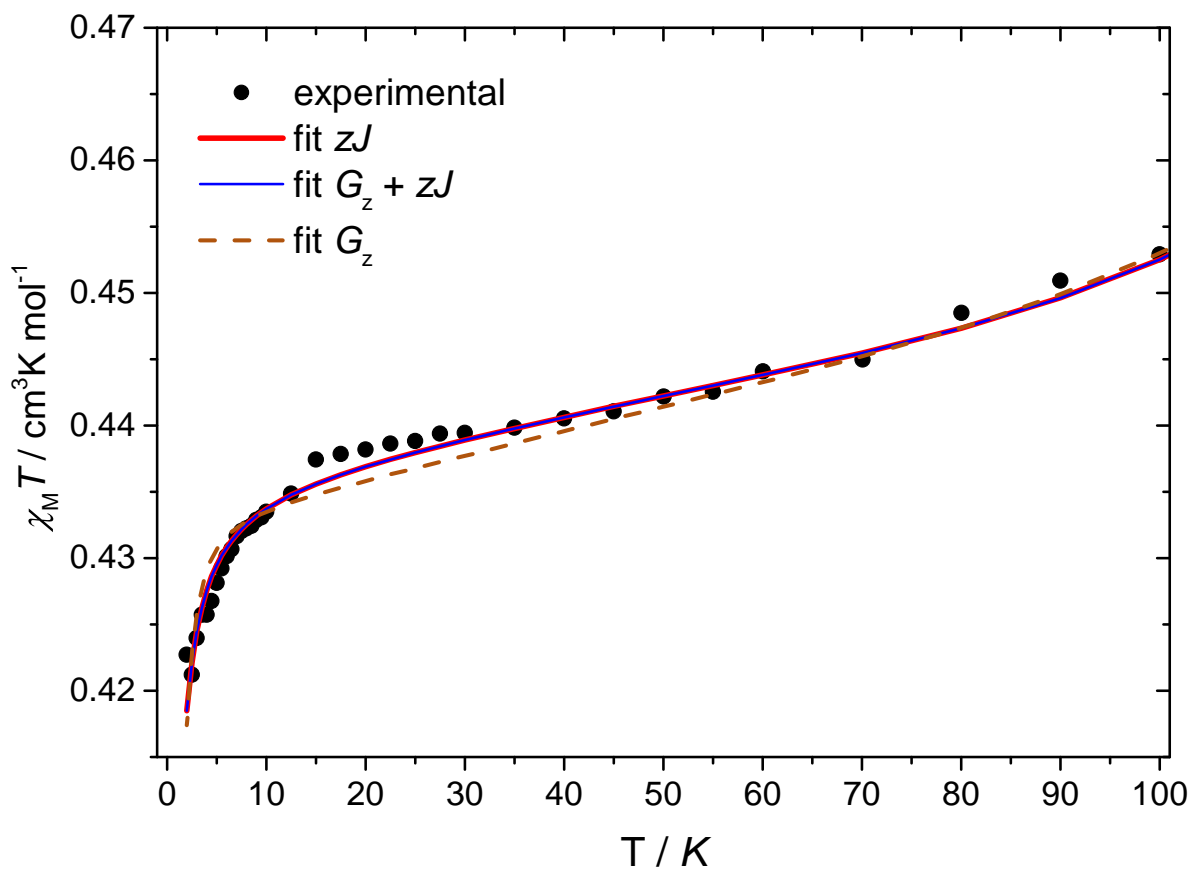
Fig. S13: Experimental χT curve (black dots) from 2–100 K together with the corresponding fits based on mean-field intermolecular exchange zJ (red line), antisymmetric exchange interaction G_z (dashed orange line) and both effects (blue line). Note that the red and the blue line are *de facto* congruent.

S6 BS-DFT calculations

Broken-symmetry DFT (BS-DFT) calculations were performed for trinuclear model complexes for which one of the copper(II) ions is replaced by a diamagnetic zinc(II) ion. The corresponding model structures for the crystallographically independent cationic complex molecules denoted as **Cu1Cu1** and **Cu2Cu2** are depicted in Fig. S14). The atomic coordinates used for the model structures were taken from the single-crystal structure data. The position of all hydrogen atoms were optimized with the Turbomole[5] package of programs at RI-DFT[6]/BP86[7,8]/def2-SVP[9] level of theory. Within these optimizations a C_3 symmetry was used together with the replacement of all copper(II) ions by diamagnetic zinc(II) ions to achieve a faster convergence in the self-consistent field steps.

Subsequently, broken-symmetry DFT (BS-DFT) calculations were performed with ORCA v4.0.1 to investigate the intramolecular magnetic exchange.[14] For these calculations the B3-LYP hybrid functional[7,10] was employed in combination with highly polarized triple-ζ def2-TZVPP basis sets.[9] The calculations were speeded up by using the RIJCOSX method.[15] The magnetic coupling constant was obtained by Yamaguchi's approach according to eqn (S2) for an isotropic Heisenberg Hamiltonian ($\hat{H} = -J\hat{S}_1\hat{S}_2$).[16] Within these calculations the third copper(II) center has been replaced by a diamagnetic zinc(II) ion. The BS-DFT results are summarized in Table S8. Spin density plots for the high-spin and broken-symmetry solutions are depicted in Figs. S15 and S16. Additionally, a corresponding orbital transformation has been employed[17] to visualize the two magnetic orbitals of the BS state of **Cu1Cu1** and **Cu2Cu2** in Figs. S17 and S18), respectively.

$$J = \frac{2\left(E_{\text{BS}} - E_{\text{HS}}\right)}{\left\langle S_{\text{HS}}^2 \right\rangle - \left\langle S_{\text{BS}}^2 \right\rangle} \tag{S2}$$

Cu1Cu1   **Cu2Cu2**
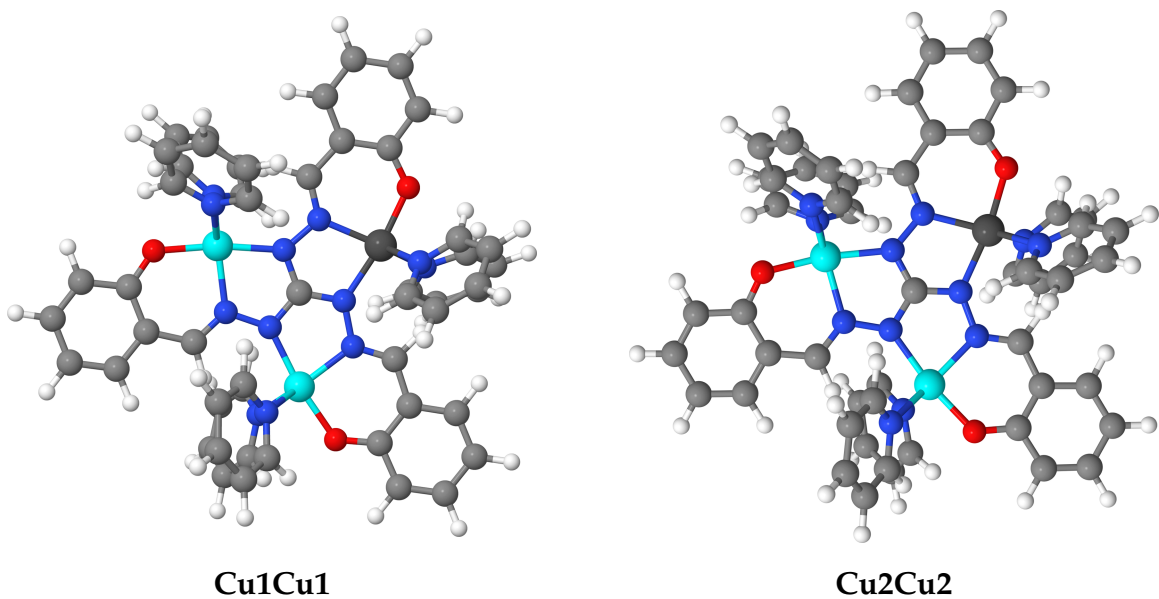
Fig. S14: Model structures [Cu$_2$Zn(saltag)(py)$_6$]$^+$ used for the BS-DFT calculations (color code: Cu – cyan; Zn – dark grey).

Table S8: BS-DFT energies, spin expectation values $\langle S^2 \rangle$, and magnetic coupling constants J according to eqn (S2).

	state	$2S+1$	E_{DFT} (a.u.)	$\langle S^2 \rangle$	J (cm^{-1})
Cu1Cu1	HS	3	−7950.89315	2.00620	−281
	BS	1	−7950.89380	0.99302	
Cu2Cu2	HS	3	−7950.89479	2.00629	−274
	BS	1	−7950.89543	0.99324	
			$J_{\text{av}} = (J_{\text{Cu1Cu1}} + J_{\text{Cu2Cu2}})/2 =$		−278

Table S9: BS-DFT energies, spin expectation values $\langle S^2 \rangle$, and magnetic coupling constants ($J = -\,^2/_3\,(E_{\text{HS}} - E_{\text{BS}})$) for a trinuclear copper(II) computational model.

	state	$2S+1$	E_{DFT} (a.u.)	$\langle S^2 \rangle$	$E_{\text{HS}} - E_{\text{BS}}$ (cm^{-1})	J (cm^{-1})
Cu1Cu1Cu1	HS	4	-7812.007434	3.759428	383	-255
	BS	2	-7812.009179	1.726949		
Cu2Cu2Cu2	HS	4	-7812.009366	3.759575	374	-249
	BS	2	-7812.011069	1.727425		
				$J_{\text{av}} = (J_{\text{Cu1Cu1Cu1}} + J_{\text{Cu2Cu2Cu2}})/2 =$		-252
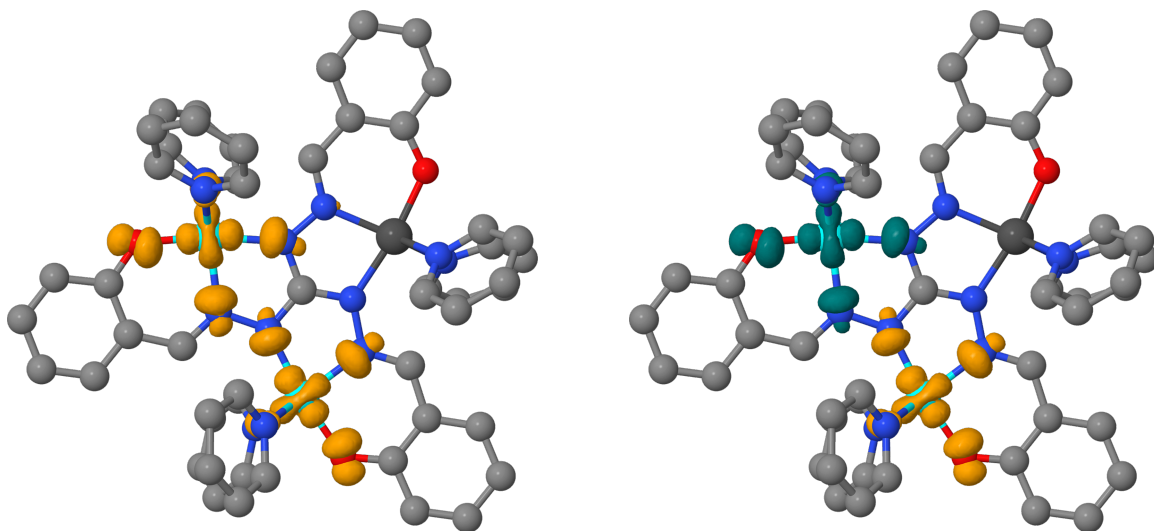
Fig. S15: Spin-density isosurfaces (0.005 au; orange = net *α* density; turquoise = net *β* density) for the high-spin (left) and broken-symmetry (right) states of **Cu1Cu1**. Hydrogen atoms are omitted for clarity.
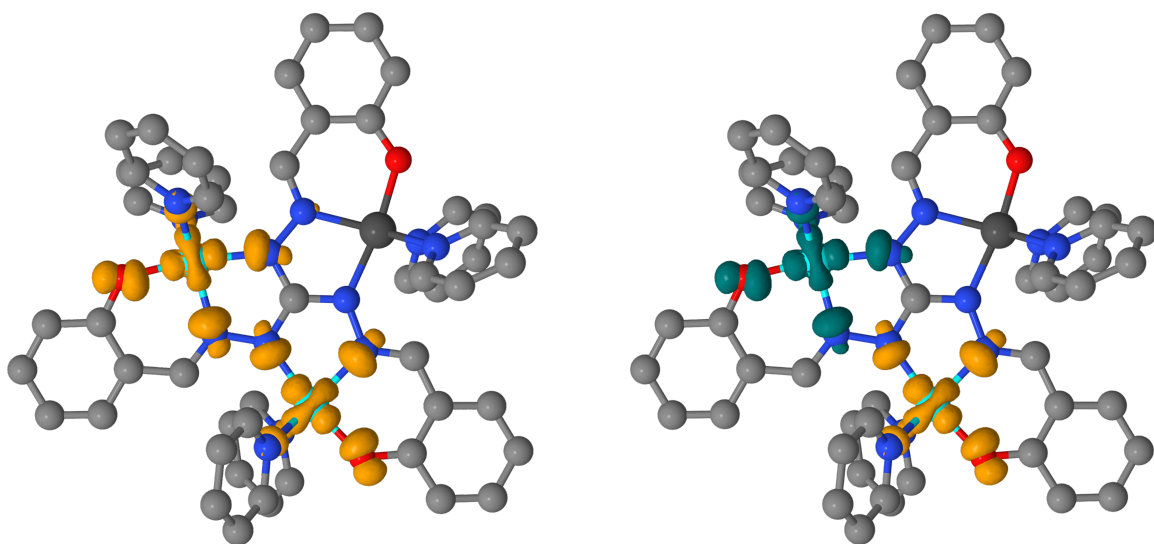
Fig. S16: Spin-density isosurfaces (0.005 au; orange = net *α* density; turquoise = net *β* density) for the high-spin (left) and broken-symmetry (right) states of **Cu2Cu2**. Hydrogen atoms are omitted for clarity.
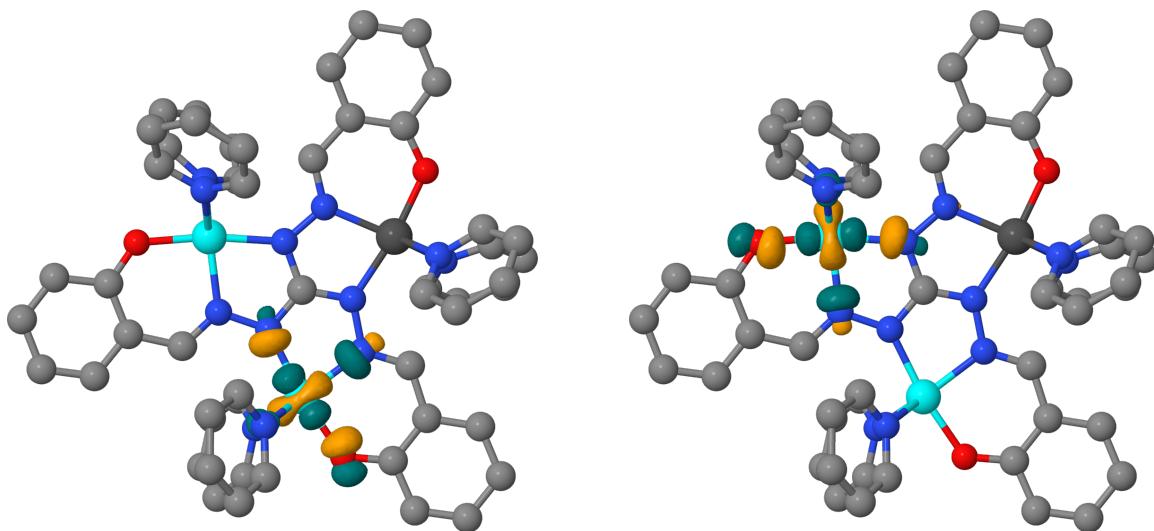
Fig. S17: Corresponding orbitals as obtained from the broken-symmetry state of **Cu1Cu1** (isosurface value: 0.06 au; overlap S = 0.113; α – left-hand side; β – right-hand side). Hydrogen atoms are omitted for clarity.
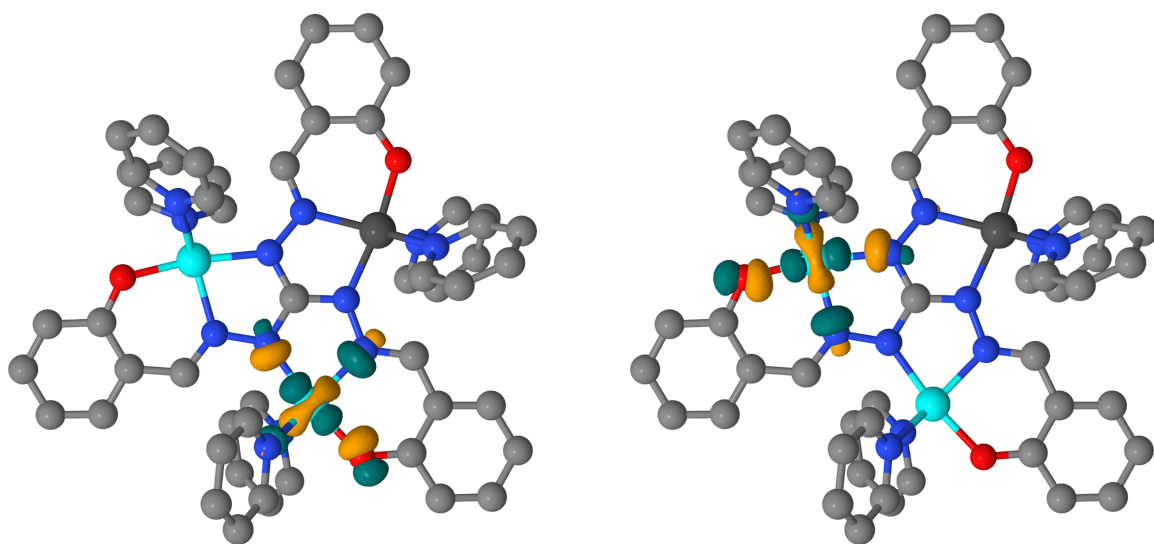
Fig. S18: Corresponding orbitals as obtained from the broken-symmetry state of **Cu2Cu2** (isosurface value: 0.06 au; spatial overlap S = 0.112; α – left-hand side; β – right-hand side). Hydrogen atoms are omitted for clarity.

S7   ESR spectroscopy

Instrumentation: Solid state ESR measurements of the ground crystalline sample were performed on a Bruker Elexsys 500 CW X-band spectrometer equipped with a He-flow cryostat. ESR measurements of frozen solutions were carried out using a commercial Bruker Elexsys 580 X-band pulsed ESR spectrometer, equipped with a ^{4}He flow cryostat for temperature control. A split-ring resonator (EN 4118X-MS3) was used for the pulsed ESR experiments. The dissolved samples are contained in standard 3 mm diameter quartz ESR tubes. In both pyridine and pyridine-d$_5$ experiments, the molecule concentration of approximately 100 μmol/L solutions were used. The relaxation times were obtained using standard Hahn-echo sequence ($\pi/2 - \tau - \pi - \tau - \text{echo}$). The pulse lengths, 16 ns for the $\pi/2$ pulse and 32 ns for the π pulse, were kept the same for all measurements.

Fit details: The ESR data were simulated using EasySpin software.[18] In all cases a line broadening parameter (lwpp) was included (12.1 mT for solid state, 7.8 mT for frozen solution) in addition to the given parameters. Features of hyperfine coupling to the copper(II) centers are missing in the ESR spectra. Nevertheless, we have tried to include the hyperfine coupling in the simulation to probe how it modifies the spectra. With an isotropic hyperfine coupling (A) up to 200 MHz, no noticeable effect can be observed in the simulated spectrum. If an anisotropic A tensor is considered, the ESR spectrum remains largely unchanged up to an $A_z = 500$ MHz due to the significant g strain associated with g_z. These hyperfine coupling values are typical for axial Cu(II). Therefore, we believe the lack of hyperfine features is due to the broad nature of the ESR resonances and no hyperfine coupling is included in the ESR analysis.
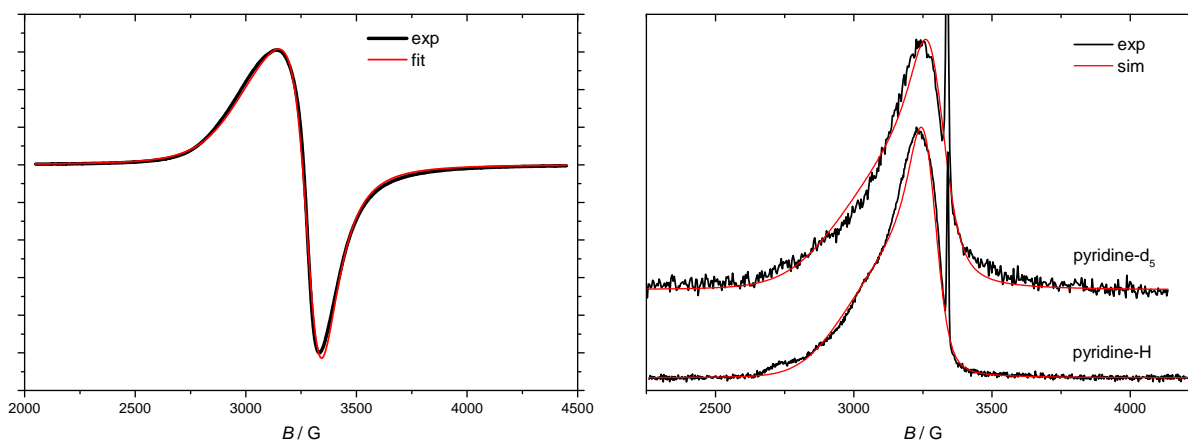
Fig. S19: Left: Solid state ESR spectrum (1st derivative) at 6 K of a powdered crystalline sample of **Cu₃saltag**, red line represents the simulated spectrum. Right: Echo-detected ESR spectra at 3 K ($\nu = 9.37$ GHz). The sharp feature around 3340 G is likely due to contaminations in the resonator and was ignored in the fitting.

Table S10: Cartesian components of the g factors as obtained by ESR spectroscopy for **Cu₃saltag**.

spectrum	parameter	x	y	z
solid	g	2.0404	2.0404	2.1889
	g_{strain}	0	0	0.2038
pyridine	g	2.0486	2.0487	2.2873
	g_{strain}	0.0011	0.0013	0.1999
pyridine-d₅	g	2.0358	2.0354	2.3020
	g_{strain}	0.00015	0.00016	0.25

S8 *Ab initio* computational results

Computational details: Atomic positions of the structures used for the *ab initio* calculations were taken from the single-crystal structure data. However, the high-level *ab initio* calculations have to be based on structural models with only one paramagnetic copper(II) center to keep the computational effort feasible. Therefore, two of the three copper ions have been replaced by zinc and all the pyridine ligands except the ones attached to the remaining copper(II) center were replaced by ammonia ligands. As a result, two *ab initio* computational models (denoted as **Cu1** and **Cu2**) with the general formula $[CuZn_2(saltag)(py)_2(NH_3)_4]^+$ were employed to obtain the single-ion properties (see Fig. S20).

Ab initio calculations were performed with the MOLCAS 8.0 SP1 package of programs.[19] For all *ab initio* calculations ANO-RCC basis sets (see Table S11) have been employed in combination with a scalar-relativistic second-order Douglas-Kroll-Hess Hamiltonian. To speed-up calculations the Cholesky decomposition of integrals was used as implemented in MOLCAS. CASSCF calculations were performed with 9 electrons in 10 orbitals (3d and 4d shell) for the ^2D multiplet. Additional dynamic correlation was treated by CASPT2 on basis of the optimized CASSCF wave function. Corresponding energies are summarized in Table S12. Subsequently, SO-RASSI calculations were carried out to take spin-orbit coupling into account (see Table S13).

A simulation of the magnetic susceptibility for both C_3 symmetric cationic complexes was performed with the POLY_ANISO program[20] employing the magnetic coupling constants obtained from BS-DFT (see Fig. S23). The corresponding g factors for the molecular framework are given in Table S15.
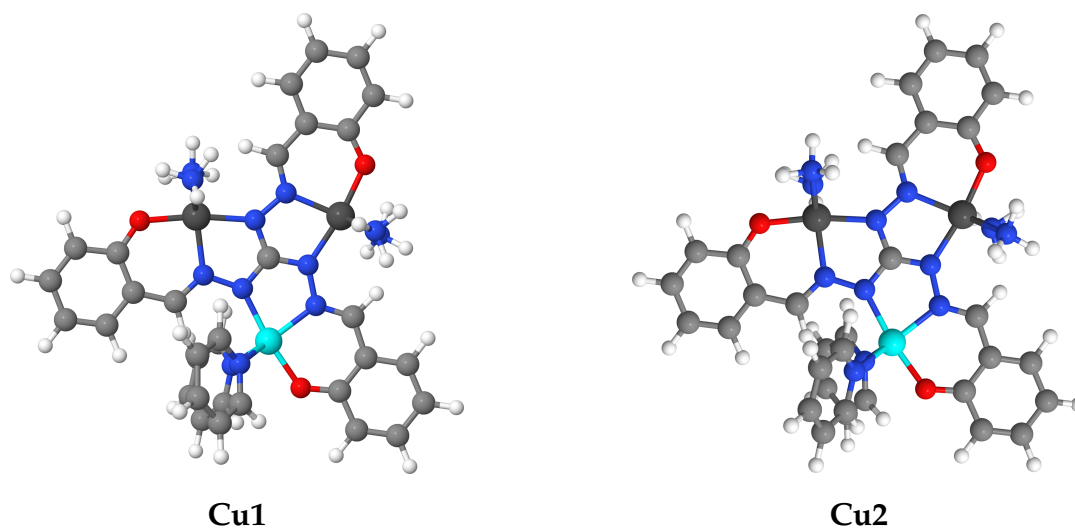
Fig. S20: Model structures $[CuZn_2(saltag)(py)_2(NH_3)_4]^+$ used for the *ab initio* calculations (color code: Cu – cyan; Zn – dark grey).

Table S11: Basis sets used for the *ab initio* calculations.

Atom	Basis set
Cu	Cu.ANO-RCC...6s5p4d2f1g.
Zn	Zn.ANO-RCC...5s4p2d.
O (donor to Cu)	O.ANO-RCC...4s3p2d1f.
O (remaining)	O.ANO-RCC...3s2p.
N (donor to Cu)	N.ANO-RCC...4s3p2d1f.
N (remaining)	N.ANO-RCC...3s2p.
C	C.ANO-RCC...3s2p.
H	H.ANO-RCC...2s.

Table S12: Relative CASSCF and CASPT2 *ab initio* energies (in cm^{-1}) for model structures **Cu1** and **Cu2** (see Fig. S20).

			Cu1		Cu2	
$2S+1$	Term	Subterm	CASSCF	CASPT2	CASSCF	CASPT2
2	^{2}D	^{2}A$'_1$	0	0	0	0
		^{2}E$'$	9440	10675	9439	10677
			10322	11853	10421	11966
		^{2}E$''$	10877	12731	10941	12867
			11023	12726	11131	12750

Table S13: Relative RASSI-SO energies (in cm^{-1}) for both crystallographically independent centers of the model structures **Cu1** and **Cu2**

Kramers doublet	Cu1	Cu2
1	0	0
2	10380	10391
3	11512	11627
4	13073	13125
5	13427	13521

Table S14: Cartesian components of the g factors for the ground-state Kramers doublet for the model structrues **Cu1** and **Cu2** ($g_{av} = (g_x + g_y + g_z)/3$)

	Cu1	Cu2
g_x	2.413	2.413
g_y	2.255	2.250
g_z	2.019	2.019
g_{av}	2.229	2.228
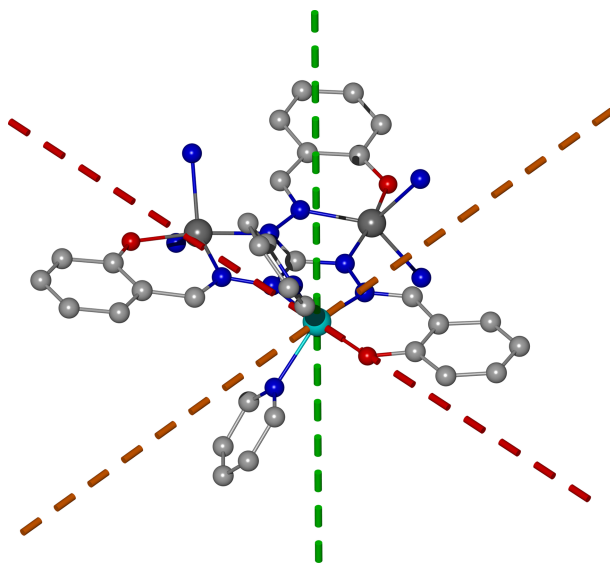
Fig. S21: Magnetic axes obtained from *ab initio* calculations for the ground state KD of a single copper(II) ion in **Cu1** indicated as dashed lines: red – hard axis (g_z), orange – intermediate axis (g_y), green – easy axis (g_x). Hydrogen atoms have been omitted for clarity (atom color code: Cu – cyan, Zn – dark grey).
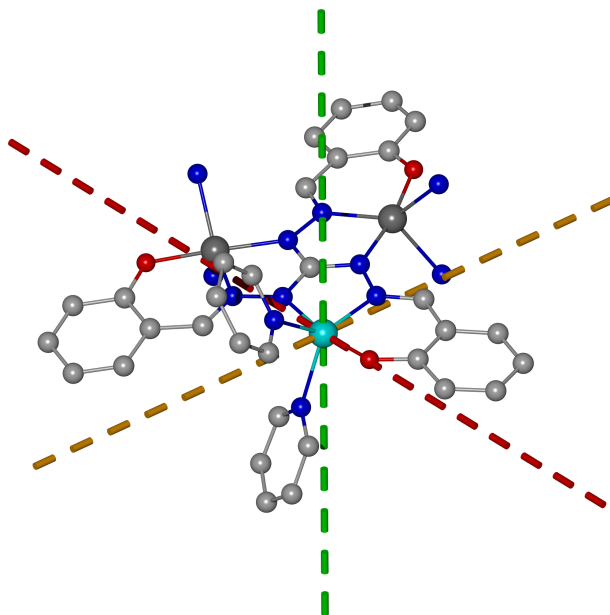
Fig. S22: Magnetic axes obtained from *ab initio* calculations for the ground state KD of a single copper(II) ion in **Cu2** indicated as dashed lines: red – hard axis (g_z), orange – intermediate axis (g_y), green – easy axis (g_x). Hydrogen atoms have been omitted for clarity (atom color code: Cu – cyan, Zn – dark grey).
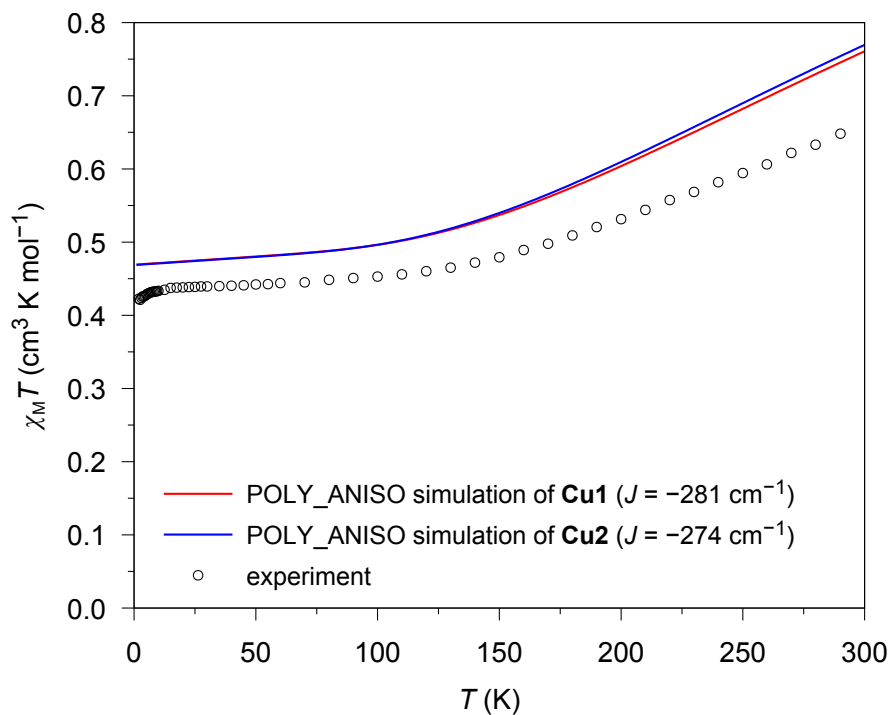
Fig. S23: Simulated temperature dependence of $\chi_M T$ based on the *ab initio* calculations of **Cu1** and **Cu2** together with the BS-DFT determined coupling constants employing the POLY_ANISO program. [20]

Table S15: Cartesian components of the g factors for the antiferromagnetic ground state of the trinuclear C_3 symmetric cationic complexes (values obtained by the POLY_ANISO program employing the model structures **Cu1** and **Cu2** together with the corresponding J values from the BS-DFT calculations)

	Cu1	**Cu2**
$g_\perp$	2.158	2.158
$g_\parallel$	2.425	2.423
g_{av}	2.247	2.246

S9 Dynamic ESR results

For experimental details and instrumentation see section S7 (ESR spectroscopy).
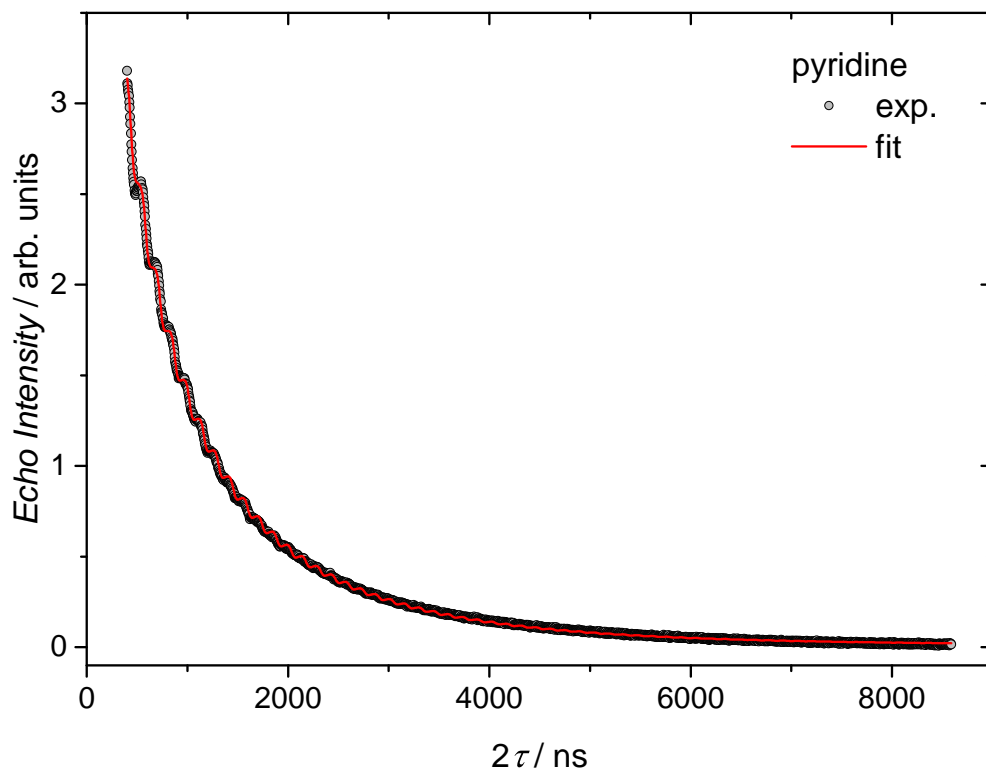
Fig. S24: Decay of the Hahn-echo intensity for **Cu$_3$saltag** in a frozen pyridine solution. The solid red line shows the best fit according to eqn (2) from the main manuscript. The fit assumes that the oscillation in the signal is due to the ESEEM effect dominated by a single harmonic at the hydrogen Zeeman frequency.[21]

References

[1] (*a*) E. Winkelmann and W. Raether, *Chem. Abstr.*, 1972, **77**, 126264; (*b*) A. Zharkouskaya, A. Buchholz and W. Plass, *Eur. J. Inorg. Chem.*, 2005, 4875–4879; (*c*) A. Zharkouskaya, H. Görls, G. Vaughan and W. Plass, *Inorg. Chem. Commun.*, 2005, **8**, 1145–1148.

[2] A. Burkhardt, T. Pakendorf, B. Reime, J. Meyer, P. Fischer, N. Stübe, S. Panneerselvam, O. Lorbeer, K. Stachnik, M. Warmer, P. Rödig, D. Göries and A. Meents, *Eur. Phys. J. Plus*, 2016, **131**, 56.

[3] W. Kabsch, *Acta Cryst.*, 2010, **D66**, 125–132.

[4] G. M. Sheldrick, *Acta Cryst.*, 2015, **C71**, 3–8.

[5] *TURBOMOLE V7.2 2017, a development of University of Karlsruhe and Forschungszentrum Karlsruhe GmbH, 1989-2007, TURBOMOLE GmbH, since 2007; available from http://www.turbomole.com.*

[6] (*a*) E. J. Baerends, D. E. Ellis and P. Ros, *Chem. Phys.*, 1973, **2**, 41–51; (*b*) B. I. Dunlap, J. W. D. Connolly and J. R. Sabin, *J. Chem. Phys.*, 1979, **71**, 3396–3402; (*c*) C. Van Alsenoy, *J. Comput. Chem.*, 1988, **9**, 620–626; (*d*) J. L. Whitten, *J. Chem. Phys.*, 1973, **58**, 4496–4501.

[7] A. D. Becke, *Phys. Rev. A: At., Mol., Opt. Phys.*, 1988, **38**, 3098–3100.

[8] J. P. Perdew, *Phys. Rev. B*, 1986, **33**, 8822–8824.

[9] F. Weigend and R. Ahlrichs, *Phys. Chem. Chem. Phys.*, 2005, **7**, 3297–3305.

[10] (*a*) C. Lee, W. Yang and R. G. Parr, *Phys. Rev. B*, 1988, **37**, 785; (*b*) A. D. Becke, *J. Chem. Phys.*, 1993, **98**, 5648–5652.

[11] S. Grimme, J. Antony, S. Ehrlich and H. Krieg, *J. Chem. Phys.*, 2010, **132**, 154104.

[12] S. Boys and F. Bernardi, *Mol. Phys.*, 1970, **19**, 553–566.

[13] N. F. Chilton, R. P. Anderson, L. D. Turner, A. Soncini and K. S. Murray, *J. Comput. Chem.*, 2013, **34**, 1164–1175.

[14] (*a*) F. Neese, *WIREs Comput. Mol. Sci.*, 2012, **2**, 73–78; (*b*) F. Neese, *WIREs Comput. Mol. Sci.*, 2017, **8**, e1327.

[15] F. Neese, F. Wennmohs, A. Hansen and U. Becker, *Chem. Phys.*, 2009, **356**, 98 – 109.

[16] (*a*) K. Yamaguchi, Y. Takahara and T. Fueno, in *Ab-initio molecular orbital studies of structure and reactivity of transition metal-oxo compounds*, Springer, 1986, pp. 155–184; (*b*) T. Soda, Y. Kitagawa, T. Onishi, Y. Takano, Y. Shigeta, H. Nagao, Y. Yoshioka and K. Yamaguchi, *Chem. Phys. Lett.*, 2000, **319**, 223–230.

[17] F. Neese, *J. Phys. Chem. Solids*, 2004, **65**, 781–785.

[18] S. Stoll and A. Schweiger, *J. Magn. Reson.*, 2006, **178**, 42–55.

[19] (*a*) G. Karlström, R. Lindh, P. Malmqvist, B. O. Roos, U. Ryde, V. Veryazov, P.-O. Widmark, M. Cossi, B. Schimmelpfennig, P. Neogrády and L. Seijo, *Comp. Mater. Sci.*, 2003, **28**, 222–239; (*b*) F. Aquilante, L. D. Vico, N. Ferré, G. Ghigo, P. Malmqvist, P. Neogrády, T. B. Pedersen, M. Pitoňák, M. Reiher, B. O. Roos, L. Serrano-Andrés, M. Urban, V. Veryazov and R. Lindh, *J. Comput. Chem.*, 2010, **31**, 224–247; (*c*) F. Aquilante, J. Autschbach, R. K. Carlson, L. F. Chibotaru, M. G. Delcey, L. D. Vico, I. F. Galván, N. Ferré, L. M. Frutos, L. Gagliardi, M. Garavelli, A. Giussani, C. E. Hoyer, G. L. Manni, H. Lischka, D. Ma, P. Å. Malmqvist, T. Müller, A. Nenov, M. Olivucci, T. B. Pedersen, D. Peng, F. Plasser, B. Pritchard, M. Reiher, I. Rivalta, I. Schapiro, J. Segarra-Martí, M. Stenrup, D. G. Truhlar, L. Ungur, A. Valentini, S. Vancoillie, V. Veryazov, V. P. Vysotskiy, O. Weingart, F. Zapata and R. Lindh, *J. Comput. Chem.*, 2015, **37**, 506–541.

[20] (*a*) L. F. Chibotaru, L. Ungur and A. Soncini, *Angew. Chem. Int. Ed.*, 2008, **120**, 4194–4197; (*b*) L. Ungur, W. Van den Heuvel and L. F. Chibotaru, *New J. Chem.*, 2009, **33**, 1224–1230; (*c*) L. F. Chibotaru, L. Ungur, C. Aronica, H. Elmoll, G. Pilet and D. Luneau, *J. Am. Chem. Soc.*, 2008, **130**, 12445–12455.

[21] A. Ardavan, O. Rival, J. J. Morton, S. J. Blundell, A. M. Tyryshkin, G. A. Timco and R. E. Winpenny, *Phys. Rev. Lett.*, 2007, **98**, 057201.